**Geomechanics and Engineering**, *Vol. 40, No. 1 (2025) 47-57*
https://doi.org/10.12989/gae.2025.40.1.047


# Soil water content estimation using electromagnetic waves with different frequency domains

Hyunsoo Lee[1a], Jong-Sub Lee[1b], Seungkwan Hong[1c] and Sang Yeob Kim*[2]

[1]*School of Civil, Environmental and Architectural Engineering, Korea University, 145, Anam-ro, Seongbuk-gu, Seoul, 02841, Republic of Korea*
[2]*Department of Fire and Disaster Prevention, Konkuk University, 268, Chungwon-daero, Chungju, 27478, Republic of Korea*

(*Received March 29, 2024, Revised November 25, 2024, Accepted December 4, 2024*)

**Abstract.** To solve various problems that require geophysical countermeasures, several efforts have been made to estimate the soil water content through electromagnetic waves. This study was aimed at evaluating water content, and following three techniques of evaluation that use electromagnetic waves were compared based on the frequency domain: electrical resistivity measured at a low frequency, time-domain reflectometry (TDR) using a band of tens of MHz to several GHz, and a hyperspectral camera using light occupied in a very high frequency band. A multivariate regression model, which incorporated both the reflectance by hyperspectral images and dielectric constant as independent variables, demonstrated improved predictive accuracy compared with a single linear regression model, which solely focuses on reflectance. However, the relationship between the polynomials was induced by comparing wavelength bands that are superior to other methods when evaluating the water content of soil through hyperspectral technology. In particular, the reflectance at approximately 970 nm recorded the highest R-squared value when the curve fitted the cubic relationship between the reflectance and water content. As hyperspectral images offer the advantage of non-contact measurements, the soil water content was estimated using hyperspectral imaging techniques that exhibit similar high R-squared value as that of TDR.

**Keywords:** dielectric constant; electrical resistivity; hyperspectral image; time domain reflectometry; water content

## 1. Introduction

Soil water content is one of the most important physical indicators of geotechnical conditions. Soil water content affects the physical and chemical properties of soil, and these changes can lead to landslides or debris flows (Ray and Jacobs 2007). Drastic changes in the water content of the soil mixture can also cause anomalous behavior of the subsurface (Birle *et al.* 2008). Moreover, the soil water content in sandy soil significantly influences both the depth and magnitude of surface and subsurface settlements (Hu *et al.* 2019, Wang *et al.* 2016). Research efforts have focused on measuring variations in water content within the substructure of road pavement systems to detect issues, such as pavement damage from frost in winter and reduced bearing capacity due to summer rainfall, which are highly related to soil moisture (Kim and Jeon 2005, Cho *et al.* 2013). To prevent such dangerous situations, subsurface water content must be properly evaluated in the field of geotechnical engineering.

Following three methods use electromagnetic waves to estimate soil water content: electrical resistivity measured at a low frequency, time-domain reflectometry (TDR) using a band of tens of MHz to several GHz, and a hyperspectral camera using light occupied in a very high frequency band (Kirkham 2014). The electrical resistivity of soil is a critical indicator of water content (Kim *et al.* 2021, Kim *et al.* 2022). The development of TDR also enables the measurement of soil water content with minimal disturbance to the soil (Hong *et al.* 2019, Park *et al.* 2023). Moreover, near-infrared (NIR) spectroscopy has been widely employed as a useful tool for analysing soil properties (Jia *et al.* 2017).

In agriculture, hyperspectral imaging technology has been adopted for sensing moisture and is broadly used for estimating vegetation conditions (Champagne *et al.* 2003, Sun 2010). There are also several research efforts in soil science where hyperspectral imaging is used to estimate the organic carbon content in soil (Tahmasbian *et al.* 2018, Sun *et al.* 2022). Furthermore, hyperspectral imaging is used for Unmanned Aerial Vehicles (UAVs) to detect large-scale sites in an area (Li *et al.* 2019). The use of UAVs equipped with hyperspectral equipment is expected to expand in the field of geoengineering (Kim *et al.* 2023). However, despite its widespread application in fields such as agriculture, hyperspectral imaging technology has not garnered significant attention in the field of geotechnical engineering. Therefore, research on this technique for estimating soil water content is limited compared to the other two conventional methods, as it has not been extensively explored.

This study was aimed at estimating the water content

*Corresponding author, Assistant Professor
E-mail: sangyeob@kku.ac.kr
[a]Graduate student
[b]Professor
[c]Professor



ISSN: 2005-307X (Print), 2092-6219 (Online)

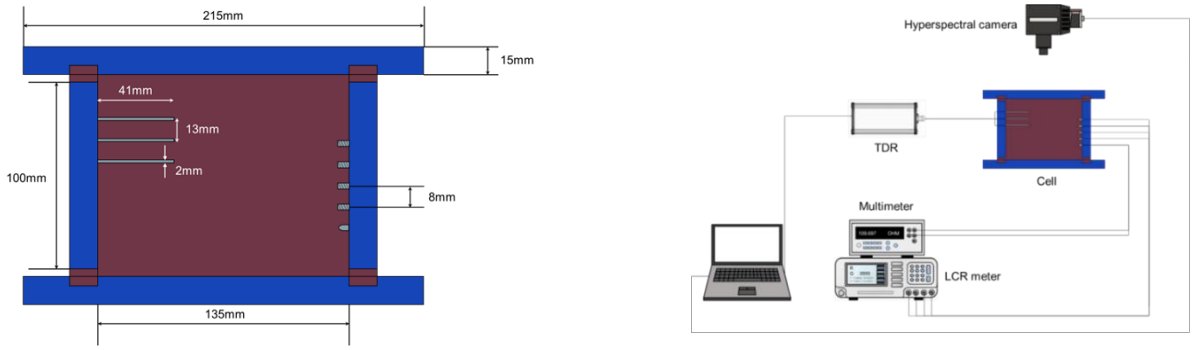


(a) MC-nylon cell (b) Measurement system

Fig. 1 MC-nylon cell equipped with TDR probes and electrodes

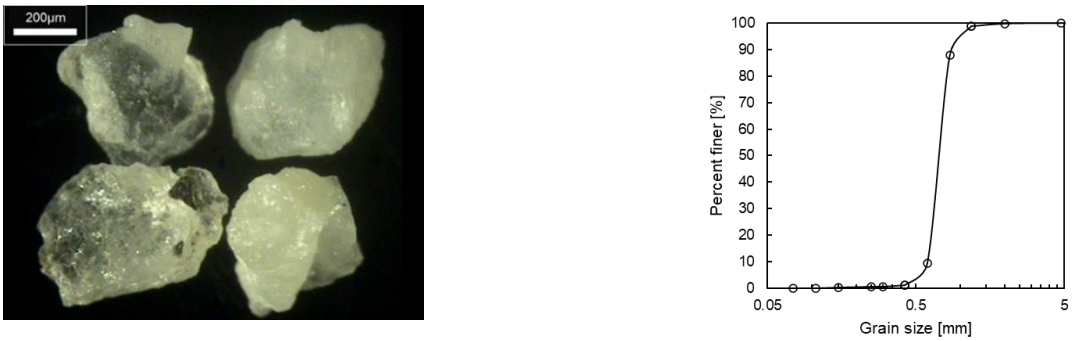


(a) Microscopic image (b) Grain size distribution curve

Fig. 2 Jumunjin standard sand (20/30)

using electromagnetic waves according to frequency. First, the properties of the sample and cell used in the experiment with the TDR probes and four electrodes for electrical resistivity are introduced. Subsequently, the reflectance obtained from the hyperspectral images and empirical electrical properties acquired by the cell are described. Finally, the water content estimation through properties including reflectance and the most effective band channel is discussed to assess the reliability of the water content.

## 2. Experimental setup

### *2.1 Measurement system*

A mono cast (MC)-nylon cell was fabricated to measure the electromagnetic waves, as shown in Figure 1. The MC-nylon mold is an effective barrier to minimize the interference from electrical noise. The cell, which was assembled by bolting, consisted of a bottom plate and four walls, each with a thickness of 15 mm. The length, width, and depth of the inner space were 100, 135, and 70 mm, respectively, and the long side of the cell was 215 mm considering the depth sensitivity of NIR reflectance in soil samples (Vasques *et al.* 2014). Measurements were performed using electrodes for electrical resistivity, TDR, and a hyperspectral camera in the same cell. $PT_{100}$ for temperature compensation in the cell was a resistance temperature detector, and both the temperature sensor and electrodes for electrical resistivity measurements were arranged at equal intervals (8 mm). The TDR sensors installed in an MC-nylon mold to measure electromagnetic waves are shown in Fig. 1(a). The conventional probe was composed of three stainless-steel rods. Each rod had a diameter of 2 mm and length of 41 mm, with a center-to-center spacing of 13 mm. Among these rods, the central rod, acting as the signal path, was connected to the inner conductor of a two-line wire (KS C IEC 60227-5), whereas the two side rods, which served as return paths, were soldered to the outer shield of the coaxial cable.

The electrical resistivity was determined using the measured electrical resistance obtained from an inductance–capacitance–resistance (LCR) meter connected to a reflectometer (Hyperlabs, HL1101), which incorporated the functionalities of a signal generator and an oscilloscope, as shown in Fig. 1(b). The reflectometer was connected to a computer to record and store measurements. To prevent mutual influence during the electrical resistivity measurement using TDR and electrodes, measurements were taken consecutively with a time difference. Hyperspectral images were obtained using a hyperspectral camera (Resonon Inc., Pika L) using a line-scanning technique.

### *2.2 Sample properties*

The sand used was Jumunjin standard sand, which was prepared according to the Korean Industrial Standard (KSL 5100), as shown in Fig. 2(a), and captured using a video microscope (Sometech, SV-35). The spectral analysis

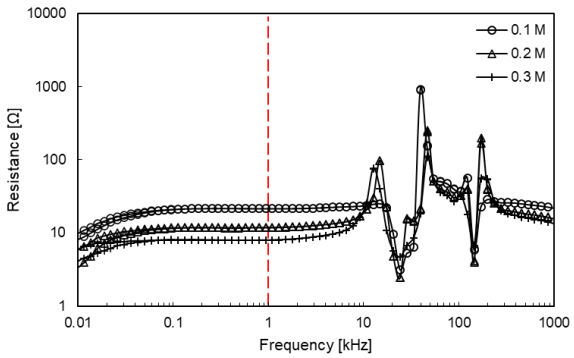


Fig. 3 Frequency sweeping using salt water

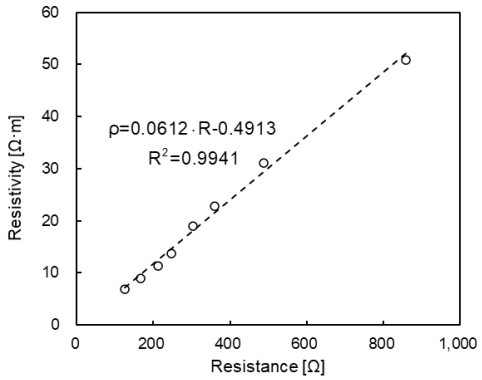


Fig. 4 Calibration result in relationship between resistivity and resistance

experiment, which involved granite soil samples obtained from four distinct regions along with kaolinite and Jumunjin standard sand, revealed that the Jumunjin standard sand samples yielded the most accurate results (Lim *et al.* 2019).

The median size of the particle $D_{50}$ was 0.72 mm with a uniform particle distribution and plotted by the grain size distribution curve, as shown in Fig. 2(b). To minimize the effect of particle size, the sand was specifically selected based on its ability to pass through a sieve with an #20 opening size of 0.85 mm while being retained on a #30 sieve with an opening size of 0.6 mm.

### *2.3 Electrical resistivity*

The electrical resistivity of soil is an important indicator of its properties, such as the degree of saturation, water content, and void ratio. (Keller and Frischknecht 1966, Lee *et al.* 2019, Santamarina *et al.* 2001, Kim *et al.* 2023). To measure the electrical resistivity of the soil, the cell was equipped with four electrodes arranged in a Wenner array as shown in Fig. 1(a). The sensitivity distribution of the array, which is flat at greater depths, is more appropriate for cells (Reynolds 1997). An LF impedance analyzer (HP Inc., 4192A), which can measure the impedance over a frequency range of 5 Hz to 13 MHz and an operating voltage range of 5 mV to 1.1 V, was used for frequency sweeping in this experiment. Through frequency sweeping, 1 kHz, which provided a stable electrical resistance, was selected as the operating frequency of the LCR meter, as shown in Fig. 3.

The electrical resistance R[Ω], was converted into an electrical resistivity ρ[$\Omega \cdot m$]. The relationship between R and ρ for the cells used in this study is described below

$$\rho = \alpha \cdot R + \beta \tag{1}$$

where ρ represents the electrical resistivity, R represents the electrical resistance; α and β are parameters experimentally determined through the calibration step. Calibration was performed based on the salt concentration, and the results of the calibration are shown in Fig. 4. The step size for the salt concentration was 0.001 molarity, and the range was 0–0.010 M (0, 0.001, 0.002, 0.003, 0.004, 0.005, 0.007, and 0.010 M).

In this experiment, the temperature was compensated. Electrical resistivity was determined by converting the electrical resistance using a resistivity probe while concurrently measuring the temperature change using a $PT_{100}$ temperature sensor. The relationship between the $PT_{100}$ resistance and temperature is represented by Eq. (2).

$$T = \gamma \cdot PT_{100} + \delta \tag{2}$$

where γ is the first shape factor of $PT_{100}$, in units of [℃ · $\Omega^{-1}$], δ is the second shape factor, in units of [℃], and $PT_{100}$ is the electrical resistance measured by $PT_{100}$ temperature sensor connected to multimeter. The laboratory temperature of 22.7℃ was set as the reference temperature.

The electrical resistance was initially temperature-compensated at the reference temperature. Subsequently, the temperature-compensated electrical resistance was converted into temperature-compensated electrical resistivity. This process allowed for accurate characterization of the electrical properties while accounting for variations in temperature. The temperature-compensated electrical resistance can be expressed in terms of temperature as follows

$$R_c = R_{22.7℃} \cdot [1 + k \cdot (T - 22.7)] \tag{3}$$

where k is a temperature factor with the unit of [$℃^{-1}$], $R_c$ is the temperature-compensated electrical resistance, and $R_{22.7℃}$ is the resistance at a temperature of 22.7℃. Substituting the compensated resistance values obtained from Eq. (3), into the R term in Eq. (1) and applying Eq. (2), the following results were obtained

$$\rho[\Omega \cdot m] = 0.0612 \cdot R[\Omega] \cdot \{1 + 0.0277 \cdot [(2.740 \cdot PT_{100}[\Omega] - 227.9) - 22.7]\} \tag{4}$$

where $PT_{100}$ is the electrical resistance measured by the $PT_{100}$ temperature sensor connected to the multimeter and R is the measured resistance.

### *2.4 Time domain reflectometry*

TDR measures electromagnetic waves propagated by a transmission line in the time domain (Noborio *et al.* 1996) and is a wide-frequency bandwidth technique (O'Connor and Dowding 1999). The TDR uses a band of tens of MHz to several GHz, and the frequency is slightly different contacting the probe with a dielectric material having an electrical discontinuity, transmitting electromagnetic pulses, and measuring the reaction that is returned and reflected.

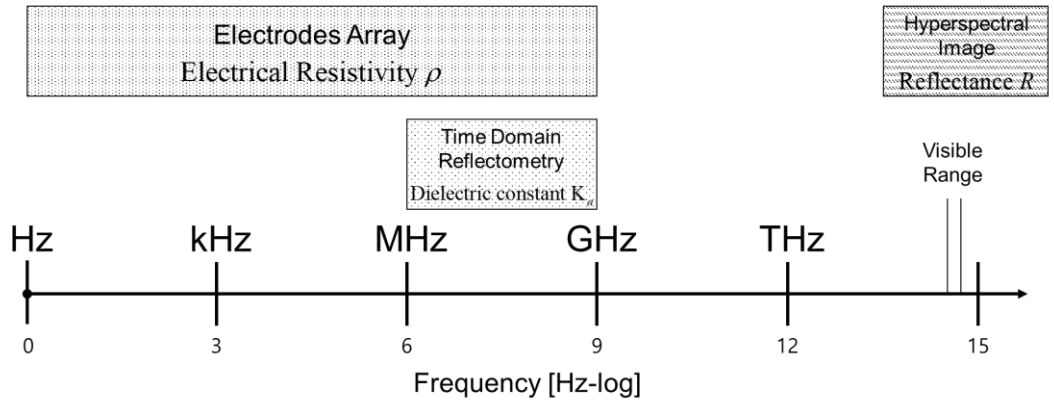


Fig. 5 Frequency range of typical methods using electromagnetic waves

To eliminate noise during signal measurements, 256 signals were averaged in the experiment.

The velocity of the electromagnetic pulse was calculated using the apparent length ($L_a$) of the electromagnetic wave and the length of the probe (L), which changed according to the dielectric constant ($K_a$) of the dielectric material in contact with the probe. The apparent length can be determined in TDR signals by the crossing point of the tangents, which is termed the tangent analysis method (Chung and Lin 2009, Lee *et al*. 2023). The relationship between the electromagnetic wave velocity (v) and dielectric constant of the soil can be expressed as

$$v = \frac{2L}{t} = \frac{c}{\sqrt{K_a}} \tag{5}$$

where t is travel time of the electromagnetic wave, L is the length of the TDR probe, and c is the velocity of the electromagnetic wave propagated in vacuum ( $3 \times 10^8\, m/s$). The dielectric constant can be calculated using the electrode length (L) and apparent length ($L_a$) of the actual TDR probe as in Eq. (6).

$$K_a = \left(\frac{c}{v}\right)^2 = \left(\frac{L_a}{L}\right)^2 \tag{6}$$

The volumetric water content ($\theta_V$) of the soil was in good agreement with the quadratic or cubic equation of the dielectric constant (Topp *et al*. 1980), and the equation of the dielectric constant is

$$\theta_V = a \cdot {K_a}^3 + b \cdot {K_a}^2 + c \cdot K_a + d \tag{7}$$

where $\theta_V$ and $K_a$ are the volumetric water content and dielectric constant of the soil, respectively, and a, b, c, and d are empirical coefficients that are dependent on the mineralogy, shape, and size of the soil particles. These coefficients were determined using a calibration process, and the experiment was conducted by varying the gravimetric water content of the samples in increments of 0, 5, 10, 15, 20, 25, 30, and 35%. The gravimetric water content was adjusted under volume-controlled conditions and converted to the volumetric water content using Eq. (8).

$$\theta_V = \frac{G_s}{1+e}\omega \tag{8}$$

where e is void ratio, ω is gravimetric water content, and $G_s$ is specific gravity of soil. Unlike estimating water content using electrical resistivity through an electrodes array, temperature correction is considered negligible in TDR techniques (Topp *et al.* 1980, Van Loon *et al*. 1995).

### *2.5 Hyperspectral images*

Hyperspectral images add spectroscopic technology to spatial information, which can be used to obtain two-dimensional image information according to the spectral band of electromagnetic waves to read the reflection or absorption between continuous wavelengths of the object. One spectral dimension was added to the two-dimensional spatial information. The resulting three-dimensional dataset is usually called a data cube or hypercube and can be obtained from hyperspectral images (Chen *et al.* 2002).

Hyperspectral imaging is a noninvasive and nondestructive method that can be used for other purposes and analyses (Sun 2010). At the same time as measuring the electrical resistivity, an image can be obtained from above the cell. A minimal concern regarding negotiations exists since it utilizes electromagnetic waves in a distinct wavelength range compared to TDR and electrodes, as shown in Fig. 5. At the uppermost section of the cell, a rail was implemented to facilitate camera tracking, whereas the cell was interconnected with the electronic equipment positioned beneath it, enabling the measurement of other properties that can be obtained through electromagnetic waves.

Line scanning imaging, which was used in the experiment, uses a two-dimensional detector arranged perpendicular to the surface of the sample to measure the light entering between the slits. Continuous spatial images were captured with the movement of the camera. A camera was installed under the rail, and scanned line-by-line. Line-scanning imaging uses a two-dimensional detector arranged perpendicular to the surface of the sample to measure the light entering between the slits. In this approach, a volume of spatial-spectral data is obtained by sequentially capturing a line of spatial information with a complete spectral range per spatial pixel (Kim *et al*. 2001). Line-scanning methods are more suitable for real-time applications than wavelength-scanning methods (Chen *et al*. 2002).

Table 1 RESONON® PIKA L hyperspectral camera specifications

| | |
|---|---|
| Spectral range [nm] | 381-1024 |
| Spectral channels [ ] | 300 |
| Spatial pixels [ ] | 900 |
| Scanning speed [cm/s] | 0.171 |
| Integration time [ms] | 85 |
| Framerate [fps] | 11.754 |

Application of the line-scanning method was preferred since the experiment in which the surface of soil sample dries requires rapidity.

Hyperspectral images have many variable bands compared to the human eye, which only requires three wavelength bands (red, green, and blue) to distinguish between colors. The camera constituting the measuring system divided the wavelength band from 381 to 1024 nm into 300 channels and collected continuous spectral information from 300 band points. Raw data obtained through a camera were expressed as brightness in each channel, and the brightness can be shown in a continuous spectrum form. The camera specifications are listed in Table 1. The information acquired through hyperspectral imaging techniques relies on light and is susceptible to thermal influences (Henrichs and Lucey 2002, Peirs *et al.* 2003). Therefore, experiments were conducted based on a reference, such as laboratory temperature at 22.7℃, to ensure consistency.

## 3. Experimental results

### *3.1 Electrical resistivity*

The experiment was conducted by varying the gravimetric water content of the samples in 5% increments of 0–35%. The electrical resistivity can be obtained by substituting the resistance value measured by the LCR meter into the temperature-compensated Eq. (4). In the dry sand ($920.74\ \Omega \cdot m$), a rapid change in electrical resistivity was observed in the section where the water content transitioned to 5% ($177.99\ \Omega \cdot m$). These results can be attributed to the substantial contrast in electrical resistivity between water and dry sand. Electrical resistivity decreases with an increase in gravimetric water content owing to the power expansion decays, and the all curve fitting correlation coefficients were greater than 0.97 where ω represents the gravimetric water content (Qiu *et al.* 2020), as shown in Fig. 6. This relationship can be expressed as

$$\rho = 232.26 \cdot e^{-0.077\omega} \quad (9)$$

As the water content continued to increase, the electrical resistivity gradually decreased; however, the rate of decline reduced compared with the lower mass water content values. This is since the water content continued to increase and reached a certain threshold, and the pores became nearly saturated with water, resulting in a well-connected conductive path. Consequently, further increase in water content slightly impact the connectivity of pore water and electrical resistivity.

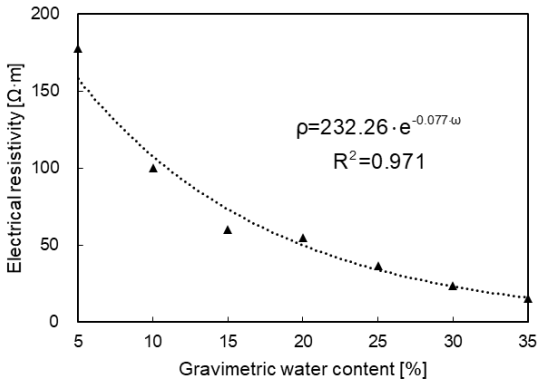


Fig. 6 The relationship between measured electrical resistivity and gravimetric water content

### *3.2 Time domain reflectometry*

The TDR probes measured the signals of the reaction by transmitting electromagnetic waves through the soil, as shown in Fig. 7(a). The dielectric constant was calculated based on the measured travel time and correlated with the volumetric water content of the soil specimen, as shown in Fig. 7(b). The volumetric water content of the soil specimen was fitted to the cubic equation of the dielectric constant in the experiment as follows

$$\theta_V = 0.011 \cdot {K_a}^3 - 0.613 \cdot {K_a}^2 + 11.678 \cdot K_a - 29.189 \quad (10)$$

The dielectric constant, also known as the relative permittivity, is defined as the ratio of the capacitance of the dielectric material present between the probes to the capacitance with a vacuum between the probes. The dielectric constant of unsaturated soil exhibits significant sensitivity to changes in water content due to the relative difference caused by large value of water (80 at 20℃). The dielectric constant of dry sand in this study was 2.8, which is similar to the reference value of 2.5 (Curtis and Defandorf 1929).

### *3.3 Hyperspectral images*

The measurement of the soil sample using the hyperspectral instrument was performed at the top of the cell,
and the instrument was framed using the line-scanning method, as shown in Fig. 8. The scanned raw data were measured as brightness in the form of a mean spectrum. The mean spectrum is the average value of the spectra of all pixels assigned for analysis in the captured image. The images were analysed using an imaging software (Resonon Inc., Spectron) after acquiring the hyperspectral data.

In general, the judgment of information in images using nontransparent materials is compared through reflectance, which is defined as follows

$$R = \frac{G}{G_0} \quad (11)$$

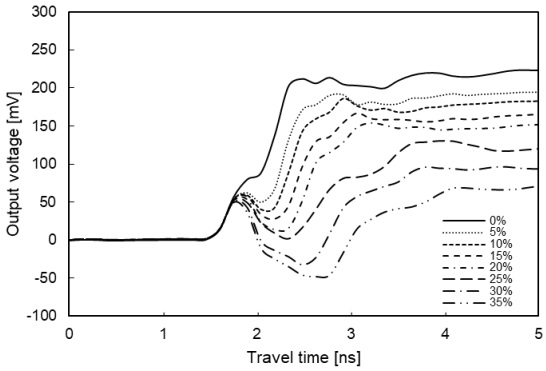


(a) TDR signals in the sand

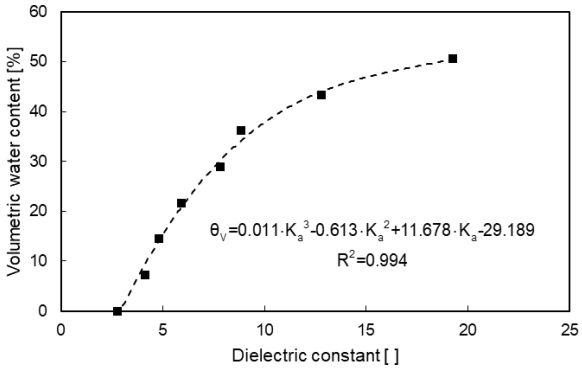


(b) Relationship between volumetric water content and the dielectric constant

Fig. 7 The results measured by TDR probes

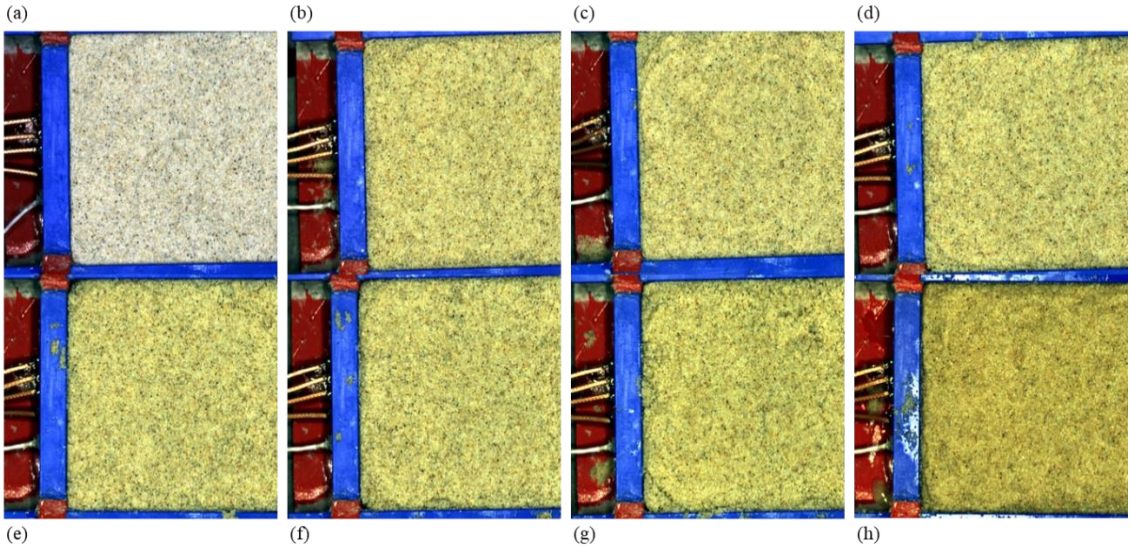


Fig. 8 Optical observation with different gravimetric water content: (a) ω=0%, (b) ω=5%, (c) ω=10%, (d) ω=15%, (e) ω=20%, (f) ω=25%, (g) ω=30% and (h) ω=35%

As a reference, $G_0$ is defined as a material that reflects very high and is also called a calibration image; G is a sample image of interest in measurement (Grahn and Geladi 2007). White correction to calibrate the highly reflective materials was performed using a Teflon plate, which is known to exhibit 99% reflectance. The reflectance calculated using the raw brightness data was normalized using the correction values. The darkness was corrected using a lens covered with a stopper to block light. The equation for calculating reflectance is also as follows, where t is the integration time (Specim.fi, 2019). In this experiment, an integration time of 85 ms was applied to all samples and reference materials.

$$R = \frac{Raw^{t1} - Dark^{t1}}{White^{t2} - Dark^{t2}} \times \frac{t2}{t1} \quad (12)$$

Pseudo-absorbance, which has no unit, is a typical term used in NIR spectroscopy (Grahn and Geladi 2007). Pseudo-absorbance has been employed to effectively determine macromolecular transport parameters of interest by utilizing the logarithm of transmitted light, achieving accurate results with minimal loss of precision (Kar *et al.* 2000) and is defined as follows

$$A = -log_{10}(R) \quad (13)$$

The mean spectrum of the captured image was converted to reflectance, as shown in Fig. 9(a), and the pseudo-absorbance is shown in Fig. 9(b). As the water content increased, the reflectance decreased. The peak value was recorded in the relatively long-wavelength region of the measured light. In the case of pseudo-absorbance, the overall shape remained similar; however, a sign change was observed at the beginning and a reversal in direction owing to the logarithmic transformation.

## 4. Analyses and discussion

### *4.1 Regression analysis*

The coefficient of determination (R-squared) is a measure of the explanatory power of the dependent variable

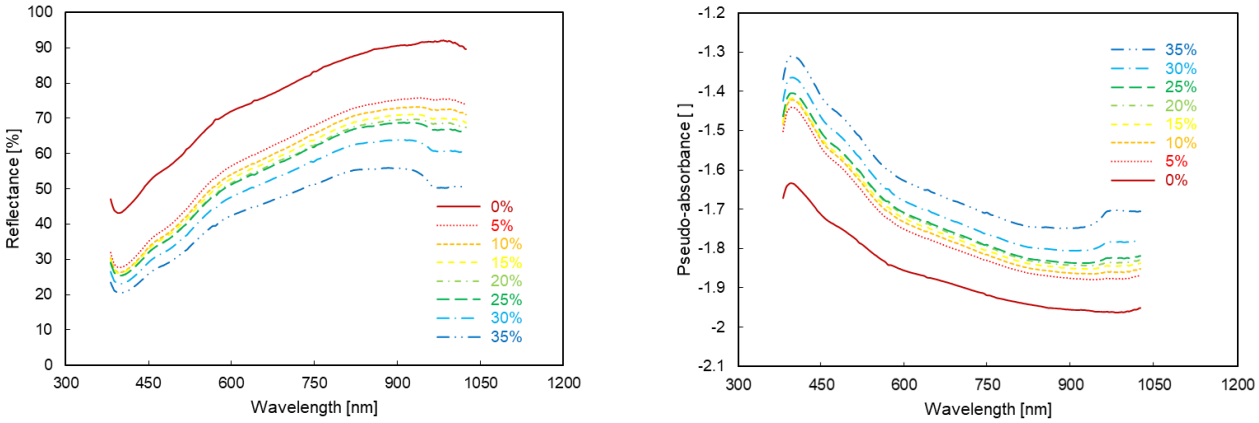


(a) Measured reflectance (b) Pseudo-absorbance

Fig. 9 The results by mean spectrum extracted from hyperspectral images

of the independent variable and is defined as follows

$$R^2 = \frac{\sum(\hat{Y}_i - \bar{Y})^2}{\sum(Y_i - \bar{Y})^2} \tag{14}$$

The total variance $(Y_i - \bar{Y})$ can be decomposed into explained variance $(\hat{Y}_i - \bar{Y})$ and unexplained variance $(Y_i - \hat{Y}_i)$ using regression equations. The R-squared is the ratio of the variance explained by the regression equation to the total variance of the dependent variable. The closer the value of the R-squared approaches 1, the greater the explanatory power of the independent variable, and the higher the fit of the estimated regression equation. The R-squared value obtained from the sample data tended to be slightly larger than that for the population. Accordingly, the degrees of freedom were reflected in the fitness of the population for the regression model to obtain the adjusted R-squared (Adj.$R^2$). All the coefficients of determination used in this study exhibited value. This is as follows

$$Adj.R^2 = R^2 - \frac{k \cdot (1 - R^2)}{n - k - 1} = 1 - \frac{\sum(Y_i - \hat{Y}_i)^2/(n - k - 1)}{\sum(Y_i - \bar{Y})^2/(n - 1)} \tag{15}$$

where n and k are the numbers of sample data and independent variables included in the regression model, respectively. A higher R-squared in a regression model indicates a stronger ability to explain the variability of the dependent variable and implies a higher potential for accurate predictions (Cook 1998, Kwak *et al.* 2022). In the experiment, independent variables, including the dielectric constant and reflectance, were generated to investigate their impact on the gravimetric water content, which is the dependent variable. To enhance accuracy and provide a comprehensive explanation or prediction of the dependent variable, multiple regression analysis was employed by incorporating these independent variables into the model.

Lim *et al.* (2019) conducted a partial least square regression (PLSR) using reflectance as a parameter to estimate the soil water content. However, the linear regression analysis yielded low R-squared values. In this experiment, the conducted PLSR analysis revealed the following R-squared values: (1) when using reflectance at 970 nm as the sole independent variable, the R-squared

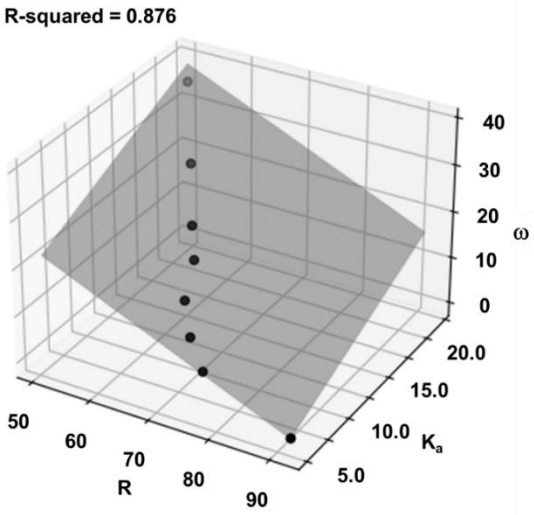


Fig. 10 A multiple linear regression analysis demonstrating the relationship between dielectric constant, reflectance at 970 nm, and gravimetric water content

value was 0.854; (2) when using the dielectric constant as the sole independent variable, the R-squared value was 0.836. However, when the model included both the reflectance and dielectric constant as independent variables in the multiple regression analysis, the R-squared value increased slightly to 0.876, and the relationship is plotted in Fig. 10. The regression equations using these two independent variables are shown in Eq. (16).

$$Y = \alpha_1 + \beta_1 \cdot X_1 + \beta_2 \cdot X_2 + \varepsilon \tag{16}$$

where Y is the dependent variable, X is the independent variable, α and β are the coefficients of the model, and ε represents the noise (Wonnacott and Wonnacott 1977). These results suggest that incorporating both reflectance and dielectric constant into the regression model improves its predictive power.

It is more accurate when multiple linear regression analysis is performed than when performed with a single independent variable. However, the R-squared value (0.876)

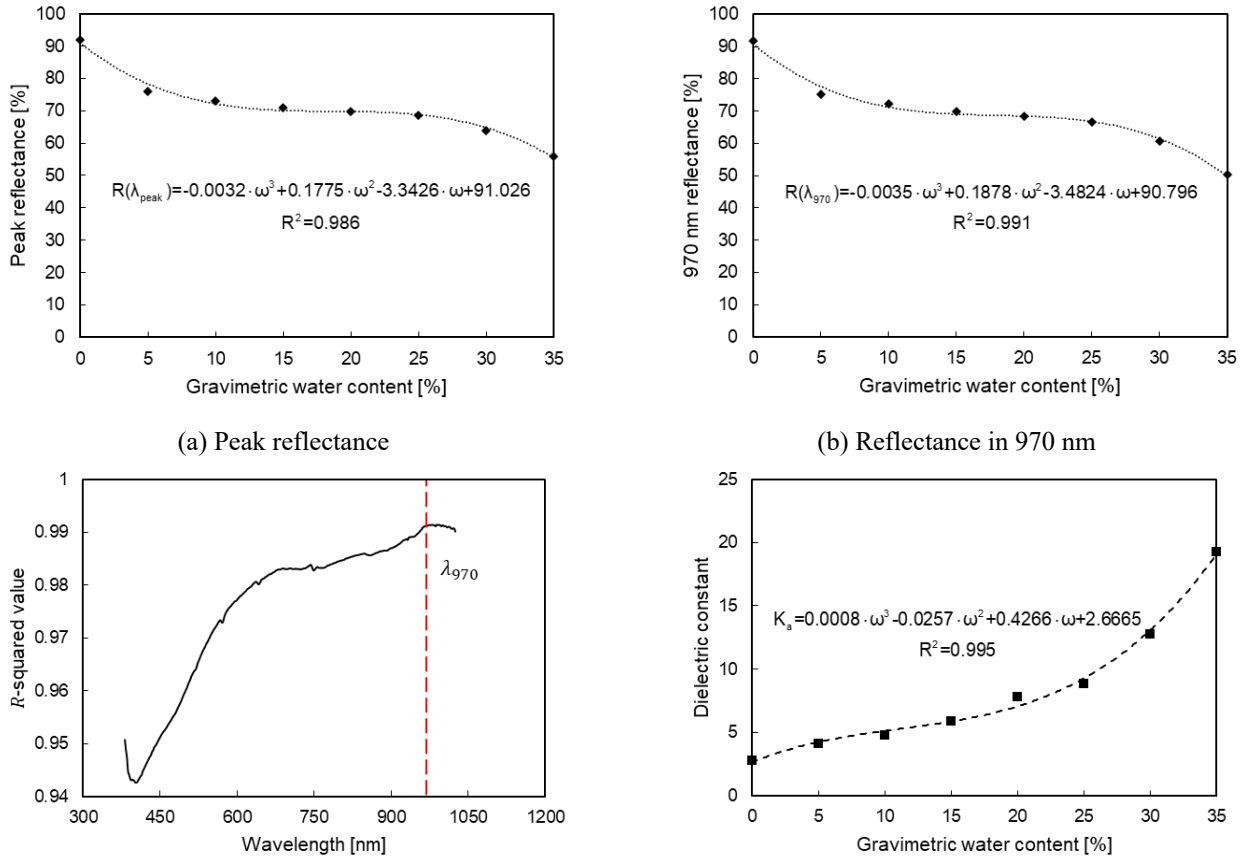


(a) Peak reflectance

(b) Reflectance in 970 nm

(c) R-squared value and wavelength channels

(d) Dielectric constant

Fig. 11 The results of relationships between: (a) peak reflectance, (b) reflectance in 970 nm and gravimetric water content, (c) curve fitting correlation coefficients and wavelength channels and (d) dielectric constant and gravimetric water content

of the multiple linear regression analysis was smaller than that (0.994) when fitting the dielectric constant and volumetric water content with a nonlinear third-order polynomial.

### *4.2 Hyperspectral images*

The soil water content can be discerned from the value of the reflectance point on a single-band channel. This value and gravimetric water content have a cubic relationship, and the equation is as follows

$$R(\lambda) = \alpha \cdot \omega^3 + \beta \cdot \omega^2 + \gamma \cdot \omega + \delta \tag{17}$$

where R is defined by single band channel, which can be dependent on the wavelength, α, β, γ, and δ are empirical coefficients that can be obtained through the experiment. The plotted relationships are shown in Figs. 11(a) and 11(b), respectively.

First, the reflectance according to water content can be discerned from the peak value. The curve-fitting correlation coefficients were greater than 0.98. The relational expression for the gravimetric water content reflecting the peak value is as follows

$$R(\lambda_{peak}) = -0.0032 \cdot \omega^3 + 0.1775 \cdot \omega^2 - 3.3426 \cdot \omega + 91.026 \tag{18}$$

The hyperspectral imaging camera used in the experiment was able to measure wavelengths in the range of 381–1024 nm. The wavelength range of approximately 381 nm corresponds to the blue light region, whereas that of approximately 1024 nm represents the NIR region, indicating different spectral domains in the electromagnetic spectrum. Furthermore, the equation can be fitted using the values measured in the same wavelength-band channel. The range (381–1024 nm) was measured by dividing it into 300 channels, and the R-squared value of the fitted graph was highest at approximately 970 nm, as shown in Fig. 11(c), which shows that the curve-fitting correlation coefficients were the highest at approximately 970 nm and the lowest in the blue light range. The curve-fitting correlation coefficients at approximately 970 nm were greater than 0.99. This paper also uses the root mean square error (RMSE), mean absolute error (MAE), and overall confidence index (OCI) to evaluate the accuracy of the prediction results. Table 2 presents the results of various indicators used to assess the goodness of fit at 970 nm.

In the field of agriculture, the 970 nm wavelength band is sensitive to water and has been used as an indicator of plant water status (Peñuelas *et al.* 1993). Accurate predictions of water content can be achieved by comparing the reflectance in the vicinity of 970 nm. The relational expression for gravimetric water content at 970 nm is as

Table 2 The results of $R^2$, RMSE, MAE, and OCI obtained by curve fitting at 970 nm

| | |
|---|---|
| $R^2$ | 0.991 |
| RMSE | 1.036 |
| MAE | 0.810 |
| OCI | 0.907 |

follows

$$R(\lambda_{970}) = -0.0035 \cdot \omega^3 + 0.1878 \cdot \omega^2 - 3.4824 \cdot \omega + 90.796 \quad (19)$$

### *4.3 Comparisons*

Fitting a polynomial function to describe the relationship between the electrical resistivity and gravimetric water content is challenging. However, applications of hyperspectral imaging techniques and TDR results in high R-squared value. The volumetric water content ($\theta_V$) of the soil agreed well with both the quadratic and cubic equations of the dielectric constant (Topp *et al*. 1980). It can also be expressed as the relationship between the gravimetric water content and dielectric constant from Eq. (8).

$$\omega = a_\omega \cdot {K_a}^3 + b_\omega \cdot {K_a}^2 + c_\omega \cdot K_a + d_\omega \quad (20)$$

where $a_\omega$, $b_\omega$, $c_\omega$, and $d_\omega$ are modified empirical coefficients from the volumetric case. However, Eq. (17) shows the relationship between the reflectance and gravimetric water content, whereas the TDR case describes the relationship between water content and dielectric constant. When the reflectance was measured, the solution to the cubic equation was the gravimetric water content, whereas when the dielectric constant was measured, the value was substituted into the cubic equation to obtain the water content. A cubic relationship between the dielectric constant and gravimetric water content also exists, as shown in Fig. 11(d). The inverted forms of the independent and dependent variables still had a polynomial relationship.

Both methods can be represented by polynomial equations; however, notable differences exist between them. The R-squared value for both methods surpassed 0.99, indicating strong goodness-of-fit. While TDR requires physical contact between the probe and sample, hyperspectral imaging technology offers the advantage of non-contact measurements. When the use of UAVs or physical contact is impractical owing to field conditions, soil water content can be estimated using hyperspectral imaging techniques that exhibit similar R-squared values. Particularly utilizing the wavelength range of 970 nm, employing lightweight hyperspectral cameras on UAVs, and leveraging straightforward calibration methods offer promising prospects for remote sensing applications (Suomalainen *et al.* 2021). Furthermore, while TDR does not account for temperature-induced effects, there is a distinction in hyperspectral imaging techniques due to their temperature dependency.

## 5. Conclusions

In this study, soil water content was measured using different electromagnetic wave techniques, depending on the frequency. Electromagnetic waves of the THz unit frequency are used in hyperspectral cameras, and time-domain reflectometry (TDR) can be evaluated in the MHz to GHz range; in the lower area, the soil water content can be evaluated through electrical resistivity. Uses of hyperspectral images and TDR were effective for comparing the water content through reflectance and the dielectric constant, respectively. The most significant observations of this study are as follows.

- Techniques for estimating the soil water content using electromagnetic waves demonstrated high reliability when curve fitting was employed. The utilization of the four electrodes of the Wenner array allowed for the accurate determination of electrical resistivity while compensating for temperature variations. Additionally, the dielectric constant, measured through TDR, served as a dependable indicator of water content.
- The reflectance through hyperspectral images and gravimetric water content can be expressed as a cubic relationship. This formula produced sufficiently reliable results since it had a high correlation coefficient of over 0.99. A multivariate regression model incorporating both the reflectance and dielectric constant as independent variables also demonstrated improved predictive accuracy compared to a single linear regression model solely focusing on reflectance. However, its predictive performance falls short of that achieved using a cubic relationship.
- Among the 300 wavelength band channels from the visible to NIR regions (381–1024 nm), the reflectance at approximately 970 nm recorded the highest R-squared value when the curve fitted a cubic relationship between reflectance and gravimetric water content. The value approached that obtained by the TDR method, whereas the hyperspectral camera remained entirely noncontact, unlike the sample-probe contact required by TDR.

## Acknowledgments

This work was supported by the National Research Foundation of Korea (NRF) grant funded by the Korea government (MIST) (No. NRF - 2021R1A5A1032433).

## References

Birle, E., Heyer, E. and Vogt, N. (2008), "Influence of the initial water content and dry density on the soil–water retention curve and the shrinkage behavior of a compacted clay", *Acta Geotech*., **3**, 191-200. https://doi.org/10.1007/s11440-008-0059-y.

Champagne, C.M., Staenz, K., Bannari, A., McNairn, H. and Deguise, J.C. (2003), "Validation of a hyperspectral curve-fitting model for the estimation of plant water content of agricultural canopies", *Remote Sens. Environ*., **87**(2), 148-160.

https://doi.org/10.1016/S0034-4257(03)00137-8.
Chen, Y.R., Chao, K. and Kim, M.S. (2002), "Machine vision technology for agricultural applications", *Comput. Electron. Agr.*, **36**(2-3), 173-191. https://doi.org/10.1016/S0168-1699(02)00100-X.
Cho, M., Lee, Y., Kim, N. and Jee, K. (2013), "Temperature Sensitivity Analysis of TDR Moisture Content Sensor for Road Pavement", *J. Korean Soc. Civil Engineers*, **33**(1), 329-336.
Chung, C.C. and Lin, C.P. (2009), "Apparent dielectric constant and effective frequency of TDR measurements: Influencing factors and comparison", *Vadose Zone J.*, **8**(3), 548-556. https://doi.org/10.2136/vzj2008.0089.
Cook, R.D. (1998), *Regression Graphics: Ideas for Studying Regressions Through Graphics*, Wiley, New York, NY, USA.
Curtis, H.L. and Defandorf, F.M. (1929), *Dielectric constant and dielectric strength of elementary substances pure inorganic compounds, and air. International Critical Tables of Numerical Data, Physics, Chemistry and Technology, 6th edn*. McGraw-Hill, New York, NY, USA.
Grahn, H. and Geladi, P. (2007), *Techniques and Applications of Hyperspectral Image Analysis*, John Wiley & Sons, Ltd., England
Hinrichs, J.L. and Lucey, P.G. (2002), "Temperature-dependent near-infrared spectral properties of minerals, meteorites, and lunar soil", *Icarus*, **155**(1), 169-180. https://doi.org/10.1006/icar.2001.6754.
Hong, WT., Yu, J., Kim, S. and Lee, JS. (2019), "Dynamic cone penetrometer incorporated with Time Domain Reflectometry (TDR) sensors for the evaluation of water contents in sandy soils", *Sensors*, **19**(18), 3841. https://doi.org/10.3390/s19183841.
Horstrand, P., Guerra, R., Rodríguez, A., Díaz, M., López, S. and López, J.F. (2019), "A UAV platform based on a hyperspectral sensor for image capturing and on-board processing", *IEEE Access*, **7**, 66919-66938.
Hu, X., He, C., Peng, Z. and Yang, W. (2019), "Analysis of ground settlement induced by Earth pressure balance shield tunneling in sandy soils with different water contents", *Sustain. Cities Soc.*, 296-306. https://doi.org/10.1016/j.scs.2018.10.038.
Jia, S., Li, H., Wang, Y., Tong, R. and Li, Q. (2017), "Hyperspectral imaging analysis for the classification of soil types and the determination of soil total nitrogen", *Sensors*, **17**(10), 2252. https://doi.org/10.3390/s17102252.
Kang, M. (2014), "Freezing-thawing effects in sand-silt mixtures on elastic waves and electrical resistivity", Dissertation, Korea University, Seoul.
Kar, S.R., Kingsbury, J.S., Lewis, M.S., Laue, T.M. and Schuck, P. (2000), "Analysis of transport experiments using pseudo-absorbance data", *Anal. Biochemistry*, **285**(1), 135-142. https://doi.org/10.1006/abio.2000.4748.
Keller, G. and Frischknecht, F. (1966), *Electrical methods in geophysical prospecting*. Pergamon Press, New York, NY, USA.
Kim, B. and Jeon, S.I. (2005), "Development of calibration model and analysis of soil water content using time-domain reflectometry probe in LTPP sections", *J. Korean Soc. Road Engineers*, **7**(4), 103-112.
Kim, M.S., Chen, Y.R. and Mehl, P.M. (2001), "Hyperspectral reflectance and fluorescence imaging system for food quality and safety", *Transactions of the ASAE*, **44**(3), 721-729. https://doi.org/10.13031/2013.6099.
Kim, S.Y., Chun, J.K., Yeo, J.Y. and Lee, J.S. (2023), "Estimation of soil porosity in mine tailing using parameters from instrumented oedometer test", *Eng. Geol.*, **317**, 107065. https://doi.org/10.1016/j.enggeo.2023.107065.
Kim, S.Y., Kim, Y. and Lee, J.S. (2021), "Effects of frozen water content and silt fraction on unconfined compressive behavior of fill materials", *Constr. Build. Mater.*, **266**, 120912. https://doi.org/10.1016/j.conbuildmat.2020.120912.
Kim, S.Y., Kwon, D.Y., Jang, A., Ju, Y.K., Lee, J.S. and Hong, S. (2023), "A review of UAV integration in forensic civil engineering: From sensor technologies to geotechnical, structural and water infrastructure applications", *Measurement*, **224**, 113886. https://doi.org/10.1016/j.measurement.2023.113886.
Kim, S.Y., Lee, J.S., Hoang, Q.N. and Park, J. (2022), "Effect of ocean environmental particles on compressibility, electrical resistivity, and stiffness characteristics of mixtures", *Eng. Geol.*, **304**, 106675. https://doi.org/10.1016/j.enggeo.2022.106675.
Kirkham, M.B. (2014), "Principles of Soil and Plant Water Relations (Second Edition)", *Vadose Zone J.*, **5**(1), 103-122. https://doi.org/10.2136/vzj2005.0100br.
Klein, M.E., Aalderink, B.J., Padoan, R., Bruin, G. and Steemers, T.A. (2008), "Quantitative hyperspectral reflectance imaging", *Sensors*, **8**(9), 5576-5618. https://doi.org/10.3390/s8095576.
Kwak, N.S. and Ko, T.Y. (2022), "Machine learning-based regression analysis for estimating Cerchar abrasivity index", *Geomech. Eng.*, **29**(3), 219-228. https://doi.org/10.12989/gae.2022.29.3.219.
Lee, D., Lee, J.S., Byun, Y.H. and Kim, S.Y. (2023), "Application of optimized time domain reflectometry probe for estimating contaminants in saline soil", *Geomech. Eng.*, **33**(3), 291-299. https://doi.org/10.12989/gae.2023.33.3.291.
Lee, K.H., Park, J.H., Park, J., Lee, I.M. and Lee, S.W. (2019), "Electrical resistivity tomography survey for prediction of anomaly inmechanized tunneling", *Geomech. Eng.*, **19**(1), 93-104. https://doi.org/10.12989/gae.2019.19.1.093
Li, Z., Li, Z., Fairbairn, D., Li, N., Xu, B. and Feng, H. (2019), "Multi-LUTs method for canopy nitrogen density estimation in winter wheat by field and UAV hyperspectral", *Comput. Electron. Agr.*, **162**, 174-182. https://doi.org/10.1016/j.compag.2019.04.005.
Lim, H., Cheon, E., Lee, D. and Lee, S. (2019), "Soil water content measurement technology using hyperspectral visible and near-infrared imaging technique", *J. Korean Geotech. Soc.*, **35**(11), 51-62. https://doi.org/10.7843/kgs.2019.35.11.51.
Lowe, A., Harrison, N. and French, A.P. (2017), "Hyperspectral image analysis techniques for the detection and classification of the early onset of plant disease and stress", *Plant Methods*, **13**(1), 1-12. https://doi.org/10.1186/s13007-017-0233-z.
Noborio, K., McInnes, K.J. and Heilman, J.L. (1996), "Measurements of soil water content, heat capacity, and thermal conductivity with a single TDR probe", *Soil Sci.*, **161**(1), 22-28.
O'Connor, K.H. and Dowding, C.H. (1999), *GeoMeasurements by Pulsing TDR Cables and Probes.* CRC Press, Florida, USA.
Oh, T.M., Cho, G.C. and Lee, C. (2014), "Effect of soil mineralogy and pore-water chemistry on the electrical resistivity of saturated soils", *J. Geotech. Geoenviron. Eng.*, **140**(11), 06014012. https://doi.org/10.1061/(ASCE)GT.1943-5606.00011.
Park, G., Kim, N., Kang, S., Kim, S.Y., Yoo, C. and Lee, J.S. (2023), "Instrumented dynamic cone penetrometer incorporated with time domain reflectometry", *Measurement*, **206**, 112337. https://doi.org/10.1016/j.measurement.2022.112337.
Peirs, A., Scheerlinck, N. and Nicolaï, B.M. (2003), "Temperature compensation for near infrared reflectance measurement of apple fruit soluble solids contents", *Postharvest Biol. Technol.*, **30**(3), 233-248. https://doi.org/10.1016/S0925-5214(03)00118-2.
Peñuelas, J., Filella, I., Biel, C., Serrano, L. and Savé, R. (1993), "The reflectance at the 950-970nm region as an indicator of plant water status", *Int. J Remote Sens.*, **14**(10), 1887-1905. https://doi.org/10.1080/01431169308954010.
Qiu, L., Yang, Y., Ma, L. and Qiao, J. (2021), "Research on the electrical resistivity characteristics of statue remolded soil", *IOP*

*Conference Series: Earth and Environmental Science*, **692**. https://doi.org/10.1088/1755-1315/692/4/042076.

Ray, R.L. and Jacobs, J.M. (2007), "Relationships among remotely sensed soil moisture, precipitation, and landslide events", *Nat. Hazards*, **43**, 211-222. https://doi.org/10.1007/s11069-006-9095-9.

Reynolds, J.M. (1997), *An introduction to applied and environmental geophysics.* John Wiley and sons, England.

Santamarina, J.C., Klein, K.A. and Fam, M.A. (2001), *Soils and waves – particulate materials behavior, characterization, and process monitoring*. Wiley, New York, NY. USA.

Specim.fi. (2019), Datacube. [online] Available at: https://www.specim.fi/iq/manual/software/iq/topics/data-cube.html.

Suomalainen, J., Oliveira, R.A., Hakala, T., Koivumäki, N., Markelin, L., Näsi, R. and Honkavaara, E. (2021), "Direct reflectance transformation methodology for drone-based hyperspectral imaging", *Remote Sens. Environ*., **266**, 112691. https://doi.org/10.1016/j.rse.2021.112691.

Sun, D.W. (2010), *Hyperspectral Imaging for Food Quality Analysis and Control.* Elsevier, USA.

Sun, W., Liu, S., Zhang, X. and Li, Y. (2022), "Estimation of soil organic matter content using selected spectral subset of hyperspectral data", *Geoderma*, **409**, 115653. https://doi.org/10.1016/j.geoderma.2021.115653.

Tahmasbian, I., Xu, Z., Boyd, S., Zhou, J., Esmaeilani, R., Che, R. and Bai, S.H. (2018), "Laboratory-based hyperspectral image analysis for predicting soil carbon, nitrogen and their isotopic compositions", *Geoderma*, **330**, 254-263. https://doi.org/10.1016/j.geoderma.2018.06.008.

Topp, G.C., Davis, J.L. and Annan, A.P. (1980), "Electromagnetic determination of soil water content: Measurements in coaxial transmission lines", *Water Resour. Res.*, **16**, 574-582. https://doi.org/10.1029/WR016i003p00574.

Vasques, G.M., Demattê, J.A.M., Rossel, R.A.V., Ramírez-López, L. and Terra, F.S. (2014), "Soil classification using visible/near-infrared diffuse reflectance spectra from multiple depths", *Geoderma*, **223**, 73-78. https://doi.org/10.1016/j.geoderma.2014.01.019.

Van Loon, W.K., Smulders, P.E., Van den Berg, C. and Van Haneghem, I.A. (1995), "Time-domain reflectometry in carbohydrate solutions", *J. Food Eng.*, **26**(3), 319-328. https://doi.org/10.1016/0260-8774(94)00064-G.

Wang, S., Qi, J., Yu, F. and Liu, Fe. (2016), "A novel modeling of settlement of foundations in permafrost regions", *Geomech. Eng.*, **10**(2), 225-245. https://doi.org/10.12989/gae.2016.10.2.225.

Wonnacott T.H. and Wonnacott, R.J. (1977), *Introductory Statistics*, Wiley, New York, NY, USA.

Yue, J., Feng, H., Jin, X., Yuan, H., Li, Z., Zhou, C., Yang, G. and Tian, Q. (2018), "A comparison of crop parameters estimation using images from UAV-mounted snapshot hyperspectral sensor and high-definition digital camera", *Remote Sens.*, **10**(7), 1138. https://doi.org/10.3390/rs10071138.